

Self-propulsive active nematics

Niels de Graaf Sousa, Simon Guldager Andersen,
Aleksandra Ardaševa, and Amin Doostmohammadi*

Niels Bohr Institute, University of Copenhagen, Copenhagen, Denmark

(Dated: September 3, 2025)

Abstract

Increasing evidence suggests that active matter exhibits instances of mixed symmetry that cannot be fully described by either polar or nematic formalism. Here, we introduce a minimal model that integrates self-propulsion into the active nematic framework. Our linear stability analyses reveal how self-propulsion shifts the onset of instability, fundamentally altering the dynamical landscape. Numerical simulations confirm these predictions, showing that self-propulsion induces anti-hyperuniform fluctuations, anomalous long-range order in vorticity, and non-universal self-similar energy cascades. Notably, these long-range ordered states emerge within the active turbulence regime well before the transition to a flocking state. Additionally, our analyses highlight a non-monotonic dependence of self-organization on self-propulsion, with optimal states characterized by a peak in correlation length. These findings are relevant for understanding of active nematic systems that self-propel, such as migrating cell layers or swarming bacteria, and offer new avenues for designing synthetic systems with tailored collective behaviours, bridging the gap between active nematics and self-propulsive systems.

I. INTRODUCTION

Active matter, encompassing systems driven far from equilibrium by internal energy dissipation, has transformed our understanding of collective dynamics in both biological and synthetic contexts [1]. From bacterial colonies [2, 3] and cellular assemblies [4, 5], to synthetic microswimmers [6, 7], active matter exhibits a remarkable variety of behaviours that challenge traditional frameworks of condensed matter physics. These systems provide a fertile arena for exploring new phases, instabilities,

* doostmohammadi@nbi.ku.dk

and emergent phenomena, enabling insights into both natural and engineered processes. Among these, active nematics – materials composed of elongated, interacting active particles – stand out for their ability to describe a wide range of experimental systems, from synthetic liquid crystals to biological tissues [8–10]. Active nematics capture hallmark features of active flows, such as defect dynamics [11], spontaneous turbulence [12], and energy transfer across scales [13, 14], making them a cornerstone in the study of active matter.

Despite their success, the active nematic framework has an inherent limitation. While it accounts for self-propulsion through active stresses, it fails to capture a crucial aspect of self-propulsion: the ability of active particles to spontaneously move along the direction of their polarity. This capability, essential to motile biological entities such as bacteria [15, 16] and motile eukaryotic cells [17, 18], e.g. sperm cells [19], introduces unique dynamics and instabilities that remain unexplored in standard active nematic formulations. These examples demonstrate that, unlike existing theoretical models which are bound by a specific individual symmetry, experimental realizations can exhibit mixed symmetry, where the nematic symmetry associated with the orientation of active particles inevitably co-exists with the polar symmetry of the particles motility.

Few theoretical studies have addressed the interplay between nematic symmetry and self-propulsion. Among these, models of self-propelled hard rods [20–23] use a set of coupled equations to describe the polarity vector and nematic tensor fields. Another notable approach, based on the polar formalism, incorporates a Frank elastic term to account for nematic inhomogeneities in the order field [24]. This model successfully predicts the emergence of both half- and full-integer topological defects. However, the absence of such self-propulsive motion in current active nematic models restricts their applicability to systems where translational self-propulsion and nematic order coexist.

Here, we introduce a simple model that integrates self-propulsion into the active nematic framework. Through linear stability analyses, we show that accounting for self-propulsion alters the instability threshold, reshaping the dynamical landscape of active nematics. Our numerical simulations validate these theoretical predictions, revealing additionally that self-propulsion triggers anti-hyperuniform fluctuations of topological defects, enhances nematic order and leads to anomalous long-range vorticity correlations, as well as non-universal self-similar energy cascades. These ordered states emerge within the active turbulence phase, preceding the transition to a flocking state. Our findings underscore the intricate relationship between self-organization and self-propulsion, with optimal states marked by a peak in correlation length.

II. METHODS

The model presented here builds on the well-established continuum representation of active nematics [13]. Particle orientation is described by the nematic director, \hat{n} , which takes into account the nematic symmetry $\hat{n} = -\hat{n}$. The nematic tensor is defined as $Q_{ij} = 2q(n_i n_j - \frac{\delta_{ij}}{2})$ with q being the magnitude of order. The nematic order parameter evolves according to the Beris–Edwards equation:

$$\partial_t Q_{ij} + (v_k + V_0 p_k) \partial_k Q_{ij} = \Gamma H_{ij} + S_{ij}. \quad (1)$$

Here, S_{ij} is the co-rotational term, which has the following form:

$$S_{ij} = (\lambda E_{ik} + \Omega_{ik})(Q_{kj} + \frac{\delta_{kj}}{2}) + (Q_{ik} + \frac{\delta_{ik}}{2})(\lambda E_{kj} - \Omega_{kj}) - 2\lambda(Q_{ij} + \frac{\delta_{ij}}{2})(Q_{kl}\partial_k v_l), \quad (2)$$

with $E_{ij} = \frac{1}{2}(\partial_i v_j + \partial_j v_i)$ and $\Omega_{ij} = \frac{1}{2}(\partial_j v_i - \partial_i v_j)$ being the strain rate and vorticity tensors, respectively. $H_{ij} = -\left(\frac{\delta \mathcal{F}}{\delta Q_{ij}}\right)$ is the molecular field that accounts for the free energy, \mathcal{F} , relaxation. The free energy contains the Landau–de Gennes expansion

with coefficient, A , and the Frank elastic term with constant, K :

$$\mathcal{F} = \int dA \left[\frac{K}{2} (\partial_k Q_{ij})^2 + A(1 - Q_{ij}Q_{ji})^2 \right]. \quad (3)$$

Additionally, we introduce in Eq. 1 a new self-advective term, $V_0 p_k$, which breaks the nematic symmetry. This term represents the self-propulsion of the particles migrating at speed V_0 , referred to as the self-propulsion speed. This is a common form of implementing self-propulsion in polar systems [25, 26], and describes self-propulsion along the polarity vector through a self-advective term. As such we expect this form of implementing self-propulsion to be applicable to systems with different mechanisms of motility generation. We take advantage of the fact that rod-shaped particles can polarize in two distinct directions and, therefore, for each active particle there are only two options for the polarity direction. In this study, we assume that active particles polarize in the direction that has the least deviation from the fluid flow. Thus, polarity is assigned to the direction of \hat{n} closest to the fluid flow, as illustrated in the schematic in Fig. 1. The assumption is based on experimental realizations that report active particles align their polarity with the fluid flow. Some examples include eukaryotic cells, such as *Dictyostelium discoideum*, [27] and epithelial monolayers, which have been observed to align the direction of their lamellipodia and consequently their intrinsic polarity with the total force acting on the cells [28]. This behaviour is also shared for bacterium, such as *Myxococcus xanthus*, where each individual particle aligns with the flow direction [29].

The fluid velocity, v_i , evolves according to the incompressible Navier-Stokes equations:

$$\rho(\partial_t v_i + v_k \partial_k v_i) = \partial_j \sigma_{ij}, \quad (4)$$

$$\partial_i v_i = 0, \quad (5)$$

where ρ is the density and σ_{ij} is the stress tensor, which has three contributions –

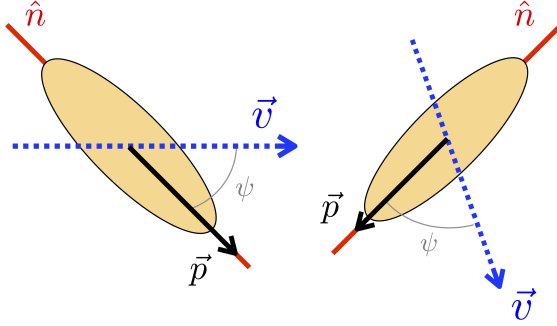


FIG. 1. **Polarity assignment mechanism.** The dotted blue arrow represents the flow velocity field, \vec{v} , the red stripe the nematic director, \hat{n} , and the black arrow shows the assigned polarity, \vec{p} . Polarity is assigned at each time step by determining which direction of \hat{n} is closest to the flow field, indicated by the angle ψ .

viscous, elastic, and active:

$$\begin{aligned} \sigma_{ij}^{\text{viscous}} &= 2\eta E_{ij}, \\ \sigma_{ij}^{\text{passive}} &= -P\delta_{ij} + 2\lambda \left(Q_{ij} + \frac{\delta_{ij}}{2} \right) Q_{lk} H_{kl} - \lambda H_{ik} \left(Q_{kj} + \frac{\delta_{kj}}{2} \right) - \lambda \left(Q_{ik} + \frac{\delta_{ik}}{2} \right) H_{kj} \\ &\quad - \partial_i Q_{kl} \frac{\delta \mathcal{F}}{\delta \partial_j Q_{lk}} + Q_{ik} H_{kj} - H_{ik} Q_{kj}, \\ \sigma_{ij}^{\text{active}} &= -\zeta Q_{ij}, \end{aligned} \tag{6}$$

with ζ being the dipolar activity coefficient, which describes the amount of ambient free energy. λ is the flow alignment coefficient and η is the fluid viscosity.

The Navier–Stokes equations (Eq. 4) are solved using the lattice Boltzmann method [30] and the advection–diffusion equation for Q_{ij} (Eq. (1)) is solved using finite-difference method. The equations are solved numerically over a square lattice of length, L , with periodic boundary conditions. The simulation variables are the following unless stated otherwise: $\rho = 40$, $\eta = 20$, $\lambda = 0.2$, $\Gamma = 0.1$, $K = 0.05$, $A = 0.1$, $L = 1024$ and $\zeta = 0.05$. For the Linear Stability section III A, the equations

have been implemented in OpenFOAM-v2306.

III. RESULTS

A. Linear Stability Analysis

To shed light on the impact of including self-propulsion effect in active nematics formulation, we perform a linear stability analysis of the nematic state for the modified equations. The classical nematic instability arises from the interplay between active stress and shear flow [31, 32]. As we shall show, accounting for self-propulsion drastically affects this instability. The dynamical variables that drive the instability are the off-diagonal nematic tensor component, Q_{xy} , and the vorticity, ω , strategically defined as $\omega = \partial_x v_y - \partial_y v_x$. The diagonal terms of the nematic tensor, Q_{xx} , are disregarded since the transverse and longitudinal modes decouple from the Jacobian matrix, as previously shown by [31].

We initialise the systems as a homogeneously ordered state along the x-axis. At zeroth order, the nematic director has the following components, $n_x = 1$ and $n_y = 0$, and the system has no net vorticity, i.e. $\phi^0 = (Q_{xx}, Q_{xy}, \omega) = (1, 0, 0)$. We apply an infinitesimal perturbation to this steady-state system, which accounts for the periodic boundary conditions on the square lattice:

$$\delta\phi^1 = \phi_{nm}(t)e^{iq(nx+my)}, \quad (7)$$

with $q = \frac{2\pi}{L}$ being the shortest wave vector in the system and L – the longitude of the system. Therefore, our set of dynamical variables with the added perturbation has the following form: $\phi(x, t) = \phi^0 + \delta\phi^1 = (1 + \delta Q_{xx}, \delta Q_{xy}, \delta\omega)$. As the system starts from an x -aligned state, the polarization takes the form $(p_x, p_y) = (1, 0)$, where we assume that the flow field has a positive x -component.

Linearizing the hydrodynamic equations reduces them to a set of coupled linear ordinary differential equations, $\partial_t \phi_{nm} = \mathcal{J}_{nm} \phi_{nm}$ (see Appendix A for details). For the instability to rise, the real part of the eigenvalues of \mathcal{J}_{nm} has to be positive. The first mode to rise is the longitudinal $(n, m) = (1, 0)$ with the following eigenvalue expression:

$$\Lambda_{10} = \frac{1}{2}q \left[-q \left(\Gamma K + \frac{\eta}{\rho} \right) - iV_0 \right. \\ \left. \pm \sqrt{q^2 \left(\Gamma K - \frac{\eta}{\rho} \right)^2 + 2qV_0 \left(\Gamma K - \frac{\eta}{\rho} \right) i - V_0^2 + \frac{2(2+\lambda)}{\rho} [\zeta - q^2 K(2+\lambda)]} \right]. \quad (8)$$

The values of V_0 that suppress the instability are given by the condition $Re[\Lambda_{10}] < 0$. As a result, one can find that the instability is suppressed above certain values of V_0^* :

$$V_0^* = \left(\Gamma K + \frac{\eta}{\rho} \right) \sqrt{\frac{(2+\lambda)}{2\Gamma K \eta} [\zeta - q^2 K(2+\lambda)] - q^2}. \quad (9)$$

This expression divides the phase space into stable and unstable regions (*black line* in Fig. 2) and shows close agreement with the results obtained from numerical simulations. This result proves that V_0 can suppress the instability and provides a new pathway on how systems can become unstable. This aligns with the results of the pure polar formalism, where self-propulsion has been shown to suppress the polar instability [25, 33].

Introducing self-propulsion allows the definition of a characteristic time scale for the nematic tensor, given by $\tau_Q = \Gamma K / V_0^2$. This can be compared to the other characteristic time scale set through the balance of active and viscous stress, $\tau_v = \eta/\zeta$. When the time scales are equal, it establishes a connection between the self-propulsion speed and the activity coefficient, $V_0 \propto \sqrt{\zeta}$. Notably, this dependency is also followed for the critical value of V_0^* , which suppresses the instability in Eq. 9,

setting a scaling relation between both variables.

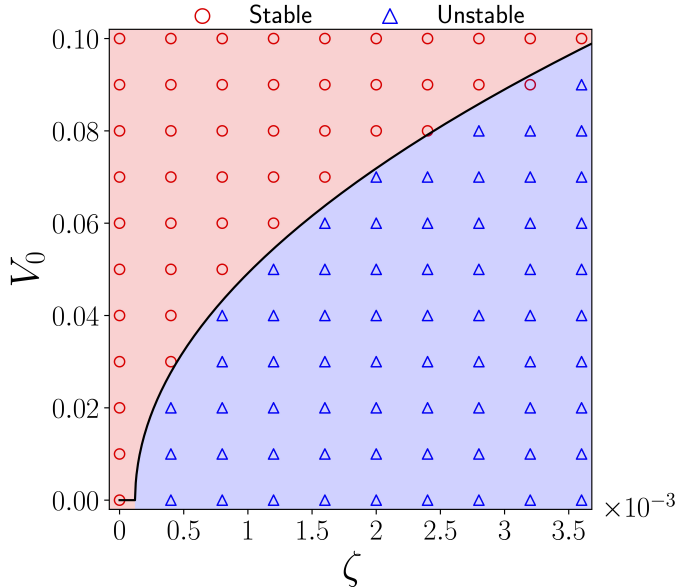


FIG. 2. Stability of the (V_0, ζ) phase space. The black line is the critical value of self-propulsion, V_0^* , needed to raise the instability Eq. 9. Scatter points are obtained through simulations: red circles indicate that the system is stable and blue triangles that the system is unstable.

B. Self-propulsion enhances order

To move beyond the linear analyses and demonstrate the effect self-propulsion has on the collective motion of active nematic, we numerically investigate the emergent dynamics. First, we consider different values of self-propulsion, V_0 . As shown in Fig. 3a–c, increasing V_0 leads to the enhancement of nematic order. In particular, the areas of nematic alignment grow and the defects become more closely spaced while being confined to the boundaries between the nematic regions. Significantly, this

effect arises at the chaotic flow regime, well before the flocking transition, with the dipolar activity coefficient set to $\zeta = 0.05$, an order of magnitude higher than the values shown in Fig. 2. To quantify the enhancement of the nematic order, we define the elastic free energy density, $\rho^e = \left\langle \frac{E}{\max(E)} \right\rangle$, with $E = \frac{K}{2}(\partial_k Q_{ij})^2$ being the elastic free energy and compute the averages over different conformations and the whole lattice (Fig. 3d). The function exhibits a convex form with the minimum occurring at $V_0 \approx 0.06$ and increasing thereafter. This indicates that the self-propulsion speed of the particles can regulate the system's order. Particularly, this order enhancement and following decay, driven by V_0 , can occur in the absence of bulk coefficients, $A = 0$ (*red line* Fig. 3d). Notably, this finding is independent of the order induced by active stress [34], demonstrating that self-propulsion alone can modulate the systems' order. Strikingly, unlike active stress, self-propulsion exhibits a non-monotonic behaviour, indicating that increasing V_0 can both enhance and break nematic order.

To further characterize the emergent nematic order, we calculate the correlation length, l_c , defined as the distance at which the autocorrelation of the nematic director, $C_{nn}(r)$, decays by a factor of e^{-1} , these measurements provide information on the average length scale over which the nematic director remains aligned. Fig. 3e presents the correlation length as a function of the self-propulsion coefficient for various system sizes, L . It is evident that as the self-propulsion coefficient V_0 , increases, the correlation length also increases, reaching a maximum at $V_0 \approx 0.06$ – the same turning point observed in the free energy density (Fig. 3d). Beyond this point, the correlation length decreases, exhibiting a concave behaviour. This indicates that self-propulsion can both establish and disrupt long-range order depending on its magnitude, irrespective of the system size. Although the correlation lengths on both sides of the maxima are similar, the system dynamics differs significantly, as is detailed in the following sections.

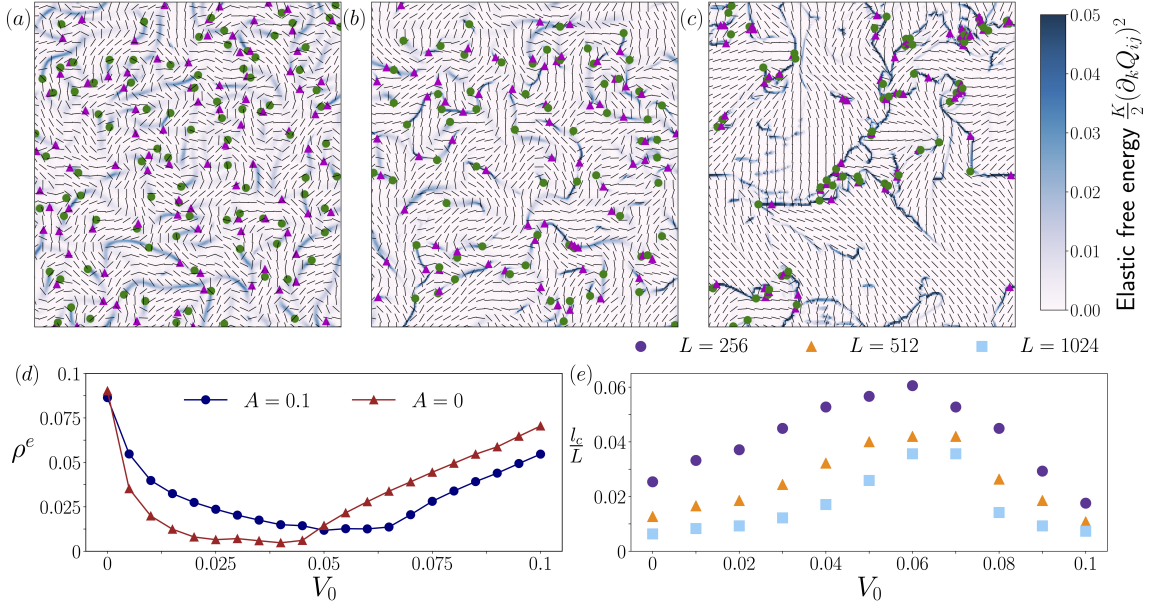


FIG. 3. Self-propulsion enhances order. Snapshots of simulations with increasing values of self-propulsion: (a) $V_0 = 0$, (b) $V_0 = 0.01$, and (c) $V_0 = 0.06$. Black lines denote the nematic director, green circles and pink triangles represent $+1/2$ and $-1/2$ topological defects, respectively. The colour denotes the magnitude of the elastic free energy, $E = \frac{K}{2}(\partial_k Q_{ij})^2$. (d) The elastic free energy density, ρ^e , as a function of self-propulsion speed, V_0 , for two different bulk free energy coefficients, $A = 0.1$ and $A = 0$. (e) Correlation length l_c as a function of self-propulsion speed V_0 for different system sizes L . l_c is defined as the distance at which the correlation function decays by a factor e^{-1} . (d–e) averaged over the lattice and different conformations.

C. Defect anti-hyperuniformity

As stated in the previous section and in Fig. 3a–c, the enhancement of nematic order is regulated by the self-propulsion speed. In this section, we show that this non-monotonic behaviour is rooted in the defect configuration, as the defects become

more closely spaced while being restricted to the boundaries of the nematic regions. Such spatial irregularity is inherently associated with hyperfluctuations and anti-hyperuniformity [26, 35], motivating us to examine the spatial behaviour of defect density fluctuations at long range.

Based on this scaling, systems of particles can be classified according to their asymptotic density fluctuation behaviour as either *uniform*, *hyperuniform* or *anti-hyperuniform*. Most disordered states of matter, e.g. ordinary fluids and amorphous solids, are uniform, meaning that $\sigma_N^2(R)$, the variance of the number of particles contained in a randomly placed spherical observation window with radius, R , scales like $\sigma_N^2(R) \sim R^{d-\alpha}$, where $\alpha = 0$, in the limit of large R . For disordered hyperuniform systems, $1 > \alpha > 0$, whereas $-d \leq \alpha < 0$ for anti-hyperuniform systems [36]. While equilibrium examples of anti-hyperuniformity are limited to systems at thermal critical points [35], many active systems exhibit this property as a manifestation of “giant number fluctuations” [26]. In this context, the relation $\sigma_N^2(R) \sim R^{d-\alpha}$ is recast as $\sqrt{\sigma_N^2(R)} = \langle N(R) \rangle^\beta$, where $\beta = 0.5(1 - \alpha/d)$ [37]. For uniform systems, $\beta = 0.5$, as predicted by the law of large numbers, whereas $\alpha < 0$ corresponds to $\beta > 0.5$, with the implication that the error on the sample mean improves more slowly than $1/\sqrt{N_{\text{samples}}}$. The scaling behaviour of density fluctuations can equivalently be described through the asymptotic behaviour of the static structure factor, S . In particular, for disordered hyperuniform and anti-hyperuniform systems, $S(\mathbf{q}) \sim |\mathbf{q}|^\alpha$ and $\sigma_N^2(R) \sim R^{d-\alpha}$ are equivalent in the infinite volume limit [35].

For every self-propulsion speed and time step, we estimate the structure factor of the corresponding defect configuration, $S(\mathbf{q})$, for all wave vectors that satisfy $|\mathbf{q}| \leq q_{\text{upper}} = 1/4$ (see Appendix B for details). These estimates are then averaged over time and orientations to obtain $\bar{S}(q)$ (Fig. 4a). The dashed horizontal line at $S = 1$ indicates the expected behaviour for the Poisson point process, and we see that for $V_0 \leq 0.02$, $(q \rightarrow 0)S(q) \propto q^\alpha$ with $\alpha \approx 0$. For $V_0 > 0.02$, $\alpha < 0$ and the

value of $\bar{S}(q)$ generally increases with V_0 . For $V_0 \geq 0.08$, however, we note that the slope of \bar{S} flattens for small q , indicating that \bar{S} might not diverge as $q \rightarrow 0$, i.e. that hyperfluctuations do not persist in the infinite-volume limit. In contrast, for $V_0 \in [0.4, 0.6]$, the slope of \bar{S} steepens for small q , suggesting that hyperfluctuations persist at long range and so that defects are in fact anti-hyperuniform for these values of V_0 .

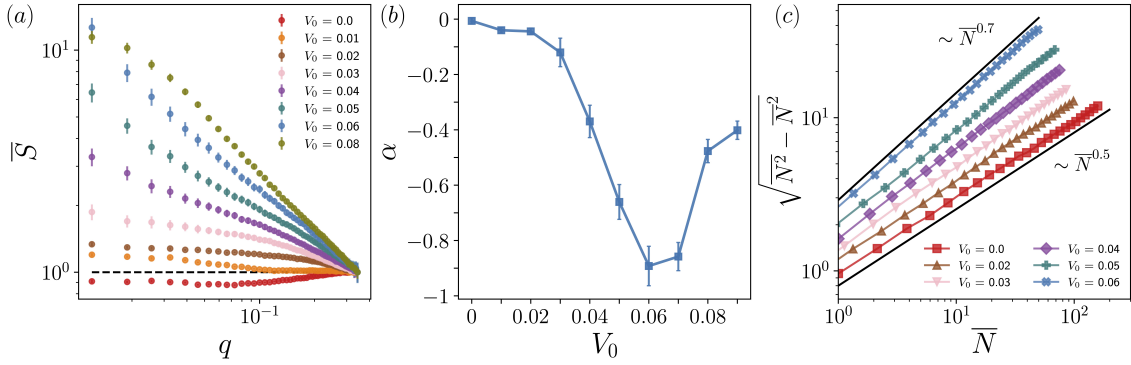


FIG. 4. Structure factor, scaling exponents, and giant number fluctuations of topological defects for $L = 1024$. (a) Normalized structure factor, \bar{S} , (averaged over orientations and time) as a function of the wave vector norm, q , across V_0 . The dashed line at $S = 1$ indicates the theoretical value of the structure factor for the Poisson process. (b) Estimated scaling exponents, α , as obtained by fitting $\bar{S}(q) \sim q^\alpha$ for small q . (c) Square root of the number variance, $(\overline{N(R)^2} - \overline{N(R)}^2)^{1/2}$, as a function of the average number of points, $\overline{N(R)}$, within a randomly placed spherical window with radius, R , for several radii, R . Giant number fluctuations with $\beta \approx 0.7 \Rightarrow \alpha \approx -0.8$ are observed for $V_0 = 0.06$, whereas for $V_0 = 0$, the expected $\beta = 1/2$ scaling of uniform systems is observed.

This difference in behaviour is reflected in the corresponding scaling exponents, α , which are obtained by fitting $S(q) \sim q^\alpha$ for small q (Fig. 4b). We see that anti-hyperuniformity is most pronounced at $V_0 = 0.06$, the self-propulsion speed of maxi-

mal order, and that the strength of anti-hyperuniformity increases as $V_0 \rightarrow 0.06$ from either side.

To directly measure defect density fluctuations, we estimate the moments of $N(R_i)$, the number of points within a randomly placed spherical observation window with radius, R_i , for 25 radii $R_i \in [L/100, L/10]$ (see Appendix C for details). As expected, the scaling of $(\sigma_N^2(R))^{1/2}$ reveals that giant number fluctuations are indeed present at $V_0 = 0.06$, with $\beta(V_0 = 0.06) \approx 0.7 \Rightarrow \alpha(V_0 = 0.06) \approx -0.8$ (Fig. 4c), in agreement with the structure factor estimate, $\alpha(V_0 = 0.06) = -0.89 \pm 0.07$. Similarly, for $V_0 = 0$ we observe the $N^{1/2}$ scaling characteristic of uniform systems.

Taken together, these findings establish that defect configurations exhibit anti-hyperuniformity and giant number fluctuations for self-propulsion speeds near $V_0 = 0.06$. Importantly, the observation that for $V_0 \in [0.04, 0.06]$, the slope of \bar{S} steepens as q is decreased suggesting that hyperfluctuations persist at long range, i.e. that these anti-hyperuniform states are intrinsic to the system and not merely finite-size effects. Strikingly, the onset and strength of anti-hyperuniformity mirror those of long-range order (Figs. 3e & 5b). This underscores the critical role of the self-propulsion speed, V_0 , in governing not only nematic order but also the spatial organization and fluctuation dynamics of topological defects.

D. Flow dynamics

Having described the effect self-propulsion has on nematic order and defect space configuration, we now consider the impact it has on the flow dynamics.

First, we perform a spectral analysis to display how the energy transfer varies from the well-known nematic energy cascade due to the self-propulsion speed. Figs. 5a & 5b show the kinetic energy spectra, $E_q \propto \int \langle |v(q)|^2 \rangle d\vec{q}$, for various self-propulsion speeds. For $V_0 = 0$, the well-established scalings are retrieved [38]. The inset plot

in Fig. 5a illustrates the scaling, $E(q) \propto q^\beta$, for small lengths ($q > 1$) as a function of V_0 demonstrating how the scaling grows linearly with self-propulsion due to the energy injection that augments the advection of the nematic tensor, describing a non-universal turbulence scaling law [39]. Furthermore, the wide range of scaling observed in the energy spectra can be compared to systems not yet fully understood theoretically, such as sperm suspensions [19], where the kinetic spectra exhibit similar small length decay as our model at certain self-propulsion speeds. The energy spectra also highlights the change of the systems' characteristic length scale from intermediate scales to large scales via a shift in the spectra maxima.

We further characterise the enstrophy spectra, $\Omega_q \propto \int \langle |w(q)|^2 \rangle d\vec{q}$, as the limit of $q \rightarrow 0$ in the enstrophy spectrum is directly related to the long-distance decay of vorticity correlations. The inset in Fig. 5b shows the decay of the vorticity correlations in real space, $\langle \omega^2(r) \rangle \propto r^{-\nu}$, for large distances ($r \rightarrow \infty$). We note that the exponent ν is related to the exponent obtained from enstrophy spectra, b , by $\nu = b + 1$ using the relation between vorticity spectrum and enstrophy, and applying Fourier relations. This vorticity scaling is very interesting and indicates that V_0 induces long-range vorticity order as the decay exponent at long distances $r \rightarrow \infty$ ($q \rightarrow 0$), $\nu < 2$, is smaller than the dimension of the system, $d = 2$. Importantly, both inset plots exhibit a change in behaviour around $V_0 = 0.06$, consistent with the critical point found during the previous sections (Figs. 3d, 3e and Fig. 4b).

For a purely nematic system, $V_0 = 0$, the system maintains its rotational symmetry invariance $\text{SO}(2)$, meaning that there is no preferred direction. However, the new term $V_0 p_k$ breaks the nematic symmetry as it assigns polarity (a direction) to the nematic director \hat{n} . To explore how introducing self-propulsion terms influences the rotational symmetry of the system we define the perpendicular and parallel coordinate system with respect to the local direction of the flow. We rotate the velocity components to this new system of coordinates: $v_x, v_y \rightarrow v_{\parallel}, v_{\perp}$. We then find the

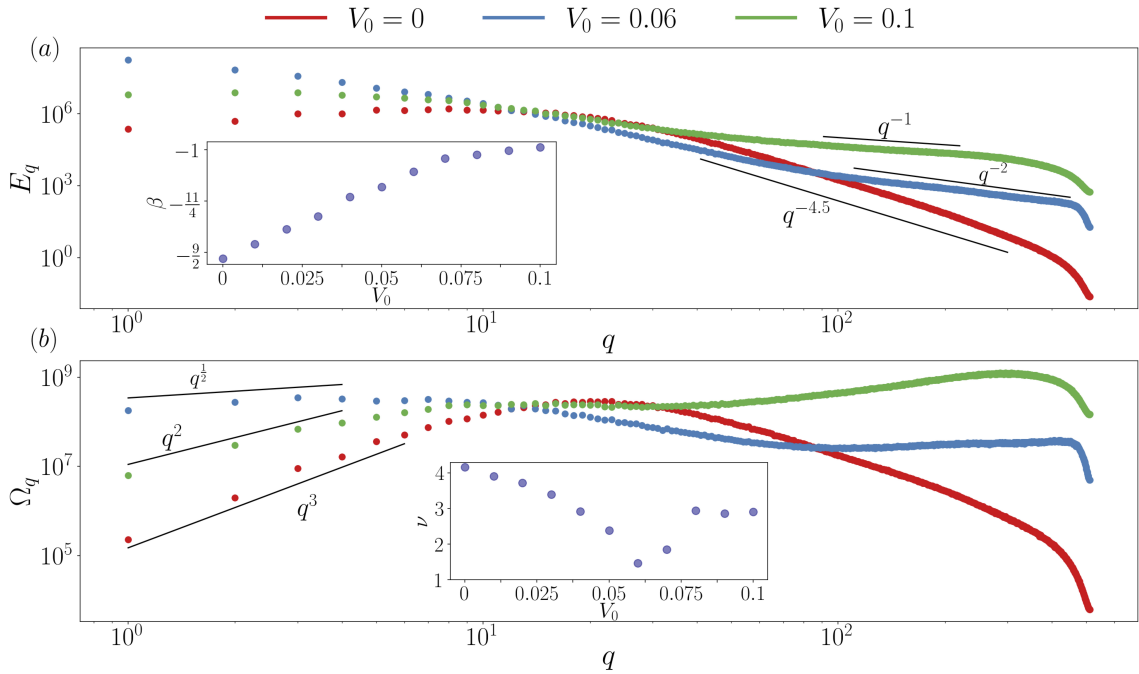


FIG. 5. **Non-universal energy cascades and anomalous long-range order.** (a) Kinetic energy spectra as a function of the wave vector, q , for different self-propulsion speeds, V_0 . Inset plot shows the scaling exponents, β , for large wave vectors as a function of V_0 , $E(q) \propto q^\beta$. (b) Enstrophy energy spectra as a function of the wave vector, q , for different self-propulsion speeds, V_0 . Inset plot shows the scaling exponents, ν , for large distances as a function of V_0 , $\langle \omega^2(r) \rangle \propto r^{-\nu}$. Wave vector has been normalized by the smallest wave vector $q = \frac{2\pi}{L}$.

autocorrelation function for both. We repeat and average this process for different lattice sites and conformations. We observe that the curves for $V_0 = 0$ and $V_0 = 0.1$ (*red and green lines* in Fig. 6) overlap greatly. This suggests that the system retains rotational symmetry. Interestingly, however, for $V_0 = 0.06$ (*blue line* in Fig. 6) the parallel and perpendicular correlations deviate from each other and

the parallel component remains correlated over longer distances than the perpendicular component, suggesting that the rotational symmetry of the system has been spontaneously broken, and the system has become anisotropic. The inset plot of Fig. 6 shows the difference between the parallel, l_{\parallel} , and perpendicular, l_{\perp} , correlation lengths as a function of V_0 . Both correlation lengths are similar for large and small self-propulsion coefficients, nonetheless for intermediate regimes the correlation lengths differ significantly. This indicates that self-propulsion, V_0 , has a re-entrant symmetry-breaking behaviour. As V_0 increases to a first threshold value, the rotational symmetry of the system is broken. However, upon further increasing V_0 to a second threshold value, the symmetry is restored. The self-propulsion values that break the systems' rotational symmetry are directly linked to those that enhance long-range order, $V_0 \approx 0.06$.

IV. CONCLUSIONS

In this study, we have developed and analysed a simple model that incorporates self-propulsion into the nematic formalism, transforming individual particles from immobile shakers into self-propulsive rods. This work is inspired by the increasing number of experimental realizations of polar particles that exhibit half-integer defects and are described using the nematic formalism despite their broken symmetry [3, 4]. Our linear stability analyses show how self-propulsion can suppress the nematic instability [31], providing new insights into the mechanisms affecting this instability. Furthermore, we demonstrate that the self-propulsion speed can regulate the systems' order, creating long-range order in a specific range of self-propulsion speeds. The emergence of larger nematic ordered regions affects the conformation of defects, which exhibit anti-hyperuniformity and giant number fluctuations near critical values. By computing energy and enstrophy spectra, we confirm the enhancement of long-range

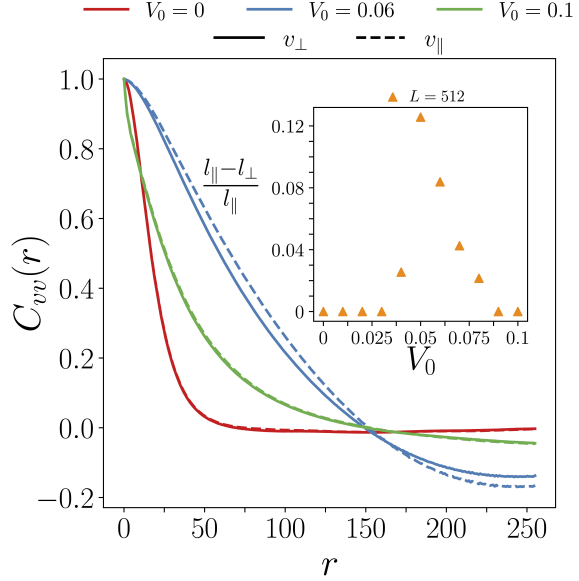


FIG. 6. **Rotational symmetry breaking.** Velocity correlation function, $C_{vv}(r)$, as a function of the radial distance for different self-propulsion coefficients, V_0 . Displayed for both the parallel, dashed line, and perpendicular velocity, continuous line, components. Averaged over different conformations. System length, $L = 512$.

order and the presence of non-universal scaling exponents. Additionally, we establish that the addition of a polar term, such as self-propulsion, can generate anisotropy and break rotational symmetry in a nematic system.

These results open new pathways for describing systems that share nematic symmetry and self-propel, such as cell tissue monolayers that exhibit nematic order while retaining some polar features like cell migration [40, 41]. This framework may also be applied to modelling bacteria, such as *Myxococcus xanthus*, that maintain their motile behaviour while aligning in either a nematic or polar manner [29] or *Pseudomonas aeruginosa*, that can polarize based on the concentration gradient along their body length [42].

Looking forward, our model provides a framework for exploring the interplay between nematic order and self-propulsion in active matter systems. Future research could focus on experimental validation of our predictions and the exploration of other polar terms that may influence nematic systems. Bridging the gap between self-propulsive and nematic systems paves the way for designing synthetic systems with tailored collective behaviours, offering exciting possibilities for advancements in materials science and biology.

COMPETING INTERESTS

We declare no competing interest.

AUTHOR CONTRIBUTIONS

A.D. designed the project. N.dG.S. performed linear stability analyses, numerical simulations, and analyses of order and flow, and S.G.A. did the hyperuniformity analyses under the supervision of A.A. and A.D. All authors contributed to the writing of the manuscript.

ACKNOWLEDGMENTS

We thank members of the Active Intelligent Matter Group for helpful comments and discussions.

FUNDING

This work was further supported by the Novo Nordisk Foundation grant no. NNF18SA0035142, NERD grant no. NNF21OC0068687 (AD), the Villum Fonden

Grant no. 29476 (AD), and the European Union via the ERC-Starting Grant PhysCoMeT (AD). A.A. acknowledges support from the EU's Horizon Europe research and innovation program under the Marie Skłodowska-Curie grant agreement No. 101063870 (TopCellComm).

Appendix A: Linear stability analysis

The Jacobian matrix is given by

$$\mathcal{J}_{nm} = \begin{bmatrix} A_{nm} & B_{nm} \\ C_{nm} & D_{nm} \end{bmatrix}, \quad (\text{A1})$$

with the components having the following form:

$$\begin{aligned} A_{nm} &= -q^2\Gamma K(n^2 + m^2) - iqV_0n, \\ B_{nm} &= \frac{\lambda}{2} \frac{n^2 - m^2}{n^2 + m^2} + 1, \\ C_{nm} &= -\frac{q^4K(n^2 + m^2)}{\rho} [n^2(2 + \lambda) + m^2(2 - \lambda)] + q^2 \frac{\zeta}{\rho} (n^2 - m^2), \\ D_{nm} &= -\frac{\eta}{\rho} q^2 (n^2 + m^2). \end{aligned} \quad (\text{A2})$$

The instability rises from the longitudinal mode, $(n, m) = (1, 0)$. When introducing it into the Eq. A1, one obtains the longitudinal Jacobian matrix:

$$\mathcal{J}_{10} = \begin{bmatrix} -q^2\Gamma K - iqV_0 & \frac{\lambda}{2} + 1 \\ -\frac{q^4K}{\rho} [(2 + \lambda)] + q^2 \frac{\zeta}{\rho} & -\frac{\eta}{\rho} q^2 \end{bmatrix}. \quad (\text{A3})$$

The eigenvalues of this matrix are given in Eq. 8.

Appendix B: Estimating the structure factor

As is common when working with long-range density fluctuations of point configurations, the spatial distribution of topological defects at steady state is assumed

to be generated by a translationally invariant and ergodic point process [35]. The former assumption entails that the pair correlation function, g_2 , satisfies $g_2(\mathbf{r}_1 + \mathbf{y}, \mathbf{r}_2 + \mathbf{y}) = g_2(\mathbf{r}_1, \mathbf{r}_2)$ for any $\mathbf{y} \in \mathbb{R}^d$ and thus $g_2(\mathbf{r}_1, \mathbf{r}_2) = g_2(\mathbf{r} = \mathbf{r}_2 - \mathbf{r}_1)$. With this assumption, the static structure factor in the infinite volume limit is given by $S(\mathbf{q}) = 1 + \rho_I \int_{\mathbb{R}^2} d\mathbf{r} (g_2(\mathbf{r}) - 1)e^{-i\mathbf{q}\cdot\mathbf{r}}$, where ρ_I is the number density in the infinite volume limit [35].

Assuming ergodicity implies that any realization of the ensemble is representative of the ensemble in the infinite volume limit, in the sense that volume averages in this limit equal the corresponding ensemble averages [35]. In particular, we can approximate ρ_I by the ensemble average of the number density $\langle \rho_N \rangle$.

On a square domain with side length, L , the infinite-volume expression for S can be estimated by [43]

$$\hat{S}(\mathbf{q}) = \frac{1}{\langle \rho_N \rangle L^2} \left| \sum_{j=1}^N e^{-i\mathbf{q}\cdot\mathbf{x}_j} \right|^2, \quad \mathbf{q} \in \mathbb{A}_L,$$

where \mathbf{x}_j refers to the point positions, \mathbb{A}_L denotes the set of allowed wavenumbers, i.e. the set of \mathbf{q} for which each component $q_i = 2\pi n/L$ for $n \in \{1, 2, \dots\}$. This estimate is asymptotically unbiased, in that the ensemble average $\langle \hat{S}(\mathbf{q}) \rangle$ converges to the true structure factor $S(\mathbf{q})$ as $L \rightarrow \infty$.

Appendix C: Estimating the local defect density and its moments

For each frame, we count the number of defects within a randomly placed spherical window centred at $\mathbf{x}_0 \in [R_{\max}, L - R_{\max}] \times [R_{\max}, L - R_{\max}]$ with radius R_i , and for computational efficiency, the centre point \mathbf{x}_0 is kept fixed while varying R_i from R_{\min} to R_{\max} . To avoid bias, the area of the union of all windows in a frame should be less than half that of the system [36], which with just one window puts an upper limit on R_{\max} as $R_{\max} = L/\sqrt{2\pi}$. Having found the number of points within a circle with

radius, R_i , for each frame, the average number of points and higher moments can be estimated empirically.

- [1] Needleman D, Dogic Z. 2017 Active matter at the interface between materials science and cell biology. *Nature Reviews Materials* **2**, 1–14. (10.1038/natrevmats.2017.48)
- [2] Aranson IS. 2022 Bacterial active matter. *Reports on Progress in Physics* **85**, 076601. (10.1088/1361-6633/ac723d)
- [3] Zhou S, Sokolov A, Lavrentovich OD, Aranson IS. 2014 Living liquid crystals. *Proceedings of the National Academy of Sciences* **111**, 1265–1270. (10.1073/pnas.1321926111)
- [4] Blanch-Mercader C, Yashunsky V, Garcia S, Duclos G, Giomi L, Silberzan P. 2018 Turbulent Dynamics of Epithelial Cell Cultures. *Physical Review Letters* **120**. (10.1103/physrevlett.120.208101)
- [5] Henkes S, Kostanjevec K, Collinson JM, Sknepnek R, Bertin E. 2020 Dense active matter model of motion patterns in confluent cell monolayers. *Nature Communications* **11**, 1405. (10.1038/s41467-020-15164-5)
- [6] Gompper G, Winkler RG, Speck T, Solon A, Nardini C, Peruani F, Löwen H, Golestanian R, Kaupp UB, Alvarez L et al.. 2020 The 2020 motile active matter roadmap. *Journal of Physics: Condensed Matter* **32**, 193001. (10.1088/1361-648X/ab6348)
- [7] Zöttl A, Stark H. 2016 Emergent behavior in active colloids. *Journal of Physics: Condensed Matter* **28**, 253001. (10.1088/0953-8984/28/25/253001)
- [8] Saw TB, Xi W, Ladoux B, Lim CT. 2018 Biological tissues as active nematic liquid crystals. *Advanced Materials* **30**, 1802579. (10.1002/adma.201802579)

- [9] Doostmohammadi A, Ladoux B. 2022 Physics of liquid crystals in cell biology. *Trends in Cell Biology* **32**, 140–150. (10.1016/j.tcb.2021.09.012)
- [10] Yaman YI, Demir E, Vetter R, Kocabas A. 2019 Emergence of active nematics in chaining bacterial biofilms. *Nature Communications* **10**, 2285. (10.1038/s41467-019-10311-z)
- [11] Giomi L, Bowick MJ, Mishra P, Sknepnek R, Cristina Marchetti M. 2014 Defect dynamics in active nematics. *Philosophical Transactions of the Royal Society A: Mathematical, Physical and Engineering Sciences* **372**, 20130365. (10.1098/rsta.2013.0365)
- [12] Alert R, Casademunt J, Joanny JF. 2022 Active Turbulence. *Annual Review of Condensed Matter Physics* **13**, 143–170. (10.1146/annurev-conmatphys-082321-035957)
- [13] Doostmohammadi A, Ignes-Mullol J, Yeomans J, Sagués F. 2018 Active nematics. *Nature Communications* **9**. (10.1038/s41467-018-05666-8)
- [14] Pearce DJ, Martínez-Prat B, Ignés-Mullol J, Sagués F. 2024 Topological defects lead to energy transfer in active nematics. *arXiv preprint arXiv:2411.18214*. (10.48550/arXiv.2411.18214)
- [15] Meacock OJ, Doostmohammadi A, Foster KR, Yeomans JM, Durham WM. 2021 Bacteria solve the problem of crowding by moving slowly. *Nature Physics* **17**, 205–210. (10.1038/s41567-020-01070-6)
- [16] Copenhagen K, Alert R, Wingreen NS, Shaevitz JW. 2021 Topological defects promote layer formation in *Myxococcus xanthus* colonies. *Nature Physics* **17**, 211–215. (10.1038/s41567-020-01056-4)
- [17] Trepaut X, Sahai E. 2018 Mesoscale physical principles of collective cell organization. *Nature Physics* **14**, 671–682. (10.1038/s41567-018-0194-9)
- [18] Kawaguchi K, Kageyama R, Sano M. 2017 Topological defects control collective dynamics in neural progenitor cell cultures. *Nature* **545**, 327–331. (10.1038/nature22321)

- [19] Creppy A, Praud O, Druart X, Kohnke PL, Plouraboué F. 2015 Turbulence of swimming sperm. *Physical Review E* **92**, 032722. (10.1103/PhysRevE.92.032722)
- [20] Baskaran A, Marchetti MC. 2008 Hydrodynamics of self-propelled hard rods. *Physical Review E—Statistical, Nonlinear, and Soft Matter Physics* **77**, 011920. (10.1103/PhysRevE.77.011920)
- [21] Baskaran A, Marchetti MC. 2012 Self-regulation in self-propelled nematic fluids. *The European Physical Journal E* **35**, 1–8. (10.1140/epje/i2012-12095-8)
- [22] Bär M, Großmann R, Heidenreich S, Peruani F. 2020 Self-Propelled Rods: Insights and Perspectives for Active Matter. *Annual Review of Condensed Matter Physics* **11**, 441–466. (10.1146/annurev-conmatphys-031119-050611)
- [23] Vafa F, Doostmohammadi A. 2025 Phase diagram, confining strings, and a new universality class in nematopolar matter. *arXiv preprint arXiv:2501.04769*. (10.48550/arXiv.2501.04769)
- [24] Amiri A, Mueller R, Doostmohammadi A. 2022 Unifying polar and nematic active matter: emergence and co-existence of half-integer and full-integer topological defects. *Journal of Physics A: Mathematical and Theoretical* **55**, 094002. (10.1088/1751-8121/ac4abe)
- [25] Giomi L, Marchetti MC. 2012 Polar patterns in active fluids. *Soft Matter* **8**, 129–139. (10.1039/c1sm06077e)
- [26] Marchetti MC, Joanny JF, Ramaswamy S, Liverpool TB, Prost J, Rao M, Simha RA. 2013 Hydrodynamics of soft active matter. *Reviews of Modern Physics* **85**, 1143–1189. Publisher: American Physical Society (10.1103/RevModPhys.85.1143)
- [27] Décauvé E, Garrivier D, Bréchet Y, Fourcade B, Bruckert F. 2003 Shear flow-induced motility of *Dictyostelium discoideum* cells on solid substrate. *Journal of Cell Science* **116**, 4331–4338. (10.1242/jcs.00726)

- [28] Peyret G, Mueller R, d'Alessandro J, Begnaud S, Marcq P, Mège RM, Yeomans JM, Doostmohammadi A, Ladoux B. 2019 Sustained oscillations of epithelial cell sheets. *Biophysical Journal* **117**, 464–478. (10.1016/j.bpj.2019.06.013)
- [29] Han E, Fei C, Alert R, Copenhagen K, Koch MD, Wingreen NS, Shaevitz JW. 2023 Local polar order controls mechanical stress and triggers layer formation in developing *Myxococcus xanthus* colonies. *ArXiv*. (10.48550/arXiv.2308.00368)
- [30] Marenduzzo D, Orlandini E, Cates ME, Yeomans JM. 2007 Steady-state hydrodynamic instabilities of active liquid crystals: Hybrid lattice Boltzmann simulations. *Physical Review E* **76**, 031921. (10.1103/PhysRevE.76.031921)
- [31] Giomi L, Mahadevan L, Chakraborty B, Hagan MF. 2012 Banding, excitability and chaos in active nematic suspensions. *Nonlinearity* **25**, 2245–2269. (10.1088/0951-7715/25/8/2245)
- [32] Santhosh S, Nejad MR, Doostmohammadi A, Yeomans JM, Thampi SP. 2020 Activity Induced Nematic Order in Isotropic Liquid Crystals. *Journal of Statistical Physics* **180**, 699–709. (10.1007/s10955-020-02497-0)
- [33] Chatterjee R, Rana N, Simha RA, Perlekar P, Ramaswamy S. 2021 Inertia Drives a Flocking Phase Transition in Viscous Active Fluids. *Physical Review X* **11**, 031063. (10.1103/PhysRevX.11.031063)
- [34] Thampi SP, Doostmohammadi A, Golestanian R, Yeomans JM. 2015 Intrinsic free energy in active nematics. *Europhysics Letters* **112**, 28004. (10.1209/0295-5075/112/28004)
- [35] Torquato S. 2018 Hyperuniform states of matter. *Physics Reports* **745**, 1–95. (10.1016/j.physrep.2018.03.001)
- [36] Torquato S, Kim J, Klatt MA. 2021 Local Number Fluctuations in Hyperuniform and Nonhyperuniform Systems: Higher-Order Moments and Distribution Functions. *Physical Review X* **11**. (10.1103/physrevx.11.021028)

- [37] Toner J, Tu Y. 1995 Long-Range Order in a Two-Dimensional Dynamical XY Model: How Birds Fly Together. *Physical Review Letters* **75**, 4326–4329. Publisher: American Physical Society (10.1103/PhysRevLett.75.4326)
- [38] Giomi L. 2015 Geometry and topology of turbulence in active nematics. *Physical Review X* **5**, 031003. (10.1103/PhysRevX.5.031003)
- [39] Bratanov V, Jenko F, Frey E. 2015 New class of turbulence in active fluids. *Proceedings of the National Academy of Sciences* **112**, 15048–15053. (10.1073/pnas.1509304112)
- [40] Saw TB, Doostmohammadi A, Nier V, Kocgozlu L, Thampi S, Toyama Y, Marcq P, Lim CT, Yeomans JM, Ladoux B. 2017 Topological defects in epithelia govern cell death and extrusion. *Nature* **544**, 212–216. (10.1038/nature21718)
- [41] d’Alessandro J, Barbier-Chebbah A, Cellerin V, Benichou O, Mège R, Voituriez R, Ladoux B. 2021 Cell migration guided by long-lived spatial memory. *Nature Communications* **12**, 4118. (10.1038/s41467-021-24249-8)
- [42] Wheeler JHR, Foster KR, Durham WM. 2024 Individual bacterial cells can use spatial sensing of chemical gradients to direct chemotaxis on surfaces. *Nature Microbiology* **9**, 2308–2322. (10.1038/s41564-024-01729-3)
- [43] Hawat D, Gautier G, Bardenet R, Lachièze-Rey R. 2023 On estimating the structure factor of a point process, with applications to hyperuniformity. *Statistics and Computing* **33**. (10.1007/s11222-023-10219-1)